Evolution and Structure of the Mesoscale Convection and Its Environment: A Case Study during the Early Onset of the Southeast Asian Summer Monsoon

Jian-Jian Wang

Goddard Center for Earth Science and Technology, University of Maryland, Baltimore County, Baltimore, and Mesoscale Atmospheric Processes Branch, NASA Goddard Space Flight Center, Greenbelt, Maryland

ABSTRACT

The evolution and structure of mesoscale convection in the South China Sea (SCS) region are documented for the first time mainly using the dual-Doppler radar dataset collected during the South China Sea Monsoon Experiment (SCSMEX) in 1998. In particular, this study focuses on the convection associated with a subtropical frontal passage during the early onset of the southeast Asian monsoon (SEAM).

For the case of 15 May 1998, interaction between the tropical monsoon flow and frontal circulation played an important role in the evolution and structure of mesoscale convection. In the prefrontal region, the southwesterly monsoon flow converged with the southwesterly frontal flow to generate northeast-to-southwest-oriented convection. In the postfrontal region, the southwesterly monsoon flow converged with the northerly frontal flow to produce a wide convective line with an east-to-west orientation. In addition, the convergence between the southerly monsoon flow and the northerly postfrontal flow generated deeper and stronger low-level convergence. The postfrontal convection was more intense and deeper than the prefrontal convection.

The precipitation and kinematic structure of mesoscale convection were studied with special attention to significant departures from archetypal tropical oceanic convection. On 15 May, prefrontal convection showed a straight upward rainfall and updraft pattern with little tilt as a result of moderate vertical wind shear. The maximum low-level convergence and updraft were 20–30 km behind instead of within 1–2 km of the leading edge. Although the convection was intense with maximum reflectivity over 50 dBZ, both pre- and postfrontal convection had a very limited stratiform region as a result of a dry environmental upper layer. The observed mesoscale convection had a tendency to form stratiform rain ahead of the convective rain, and two different modes of leading stratiform structure were found separately in pre- and postfrontal convection.

1. Introduction

The east Asian monsoon is known to be one of the most complex monsoon systems on earth and an important component of the regional and global climate. In summer, the east Asian monsoon circulation is characterized by southwesterly flow at low levels (e.g., 850 hPa) and northeasterly flow at upper levels (e.g., 200 hPa). The heavy rainfalls associated with the summer monsoon, for example, mei-yu in the Yangtze Valley of China and baiu in Japan, are important to many economic activities in the southeast and east Asian countries.

Given the importance of the east Asian summer monsoon, great attention has been given to its description and investigation. Zhu (1934) conducted a pioneering study on the relationship between the summer monsoon and the rainfall in China. Since then, numerous studies have focused on the various aspects and components of

the east Asian summer monsoon (e.g., Chang and Krishnamurti 1987) including the climatology of wind fields (e.g., Fu et al. 1983; Krishnamurti 1985; Tao and Chen 1987), the advance and retreat of the monsoon systems (e.g., Tu and Huang 1944; Ding 1994), the seasonal and annual variation of monsoon rainfall (e.g., Ninomiya and Murakami 1987; Lau et al. 1988), and the effects of the Tibetan Plateau (e.g., Murakami and Ding 1982; He et al. 1987). In addition, the mei-yu and baiu fronts in the summer monsoon season are known as the most active subtropical fronts (Ninomiya 1984). A great deal of dedicated observational and numerical studies have been conducted to study the severe rainfall events associated with the mei-yu and baiu fronts (e.g., Ninomiya and Akiyama 1971; Tao and Chen 1987; Nagata and Ogura 1991; Cho and Chen 1995; Kawatani and Takahashi 2003). The past observational studies on the mei-yu and baiu fronts can be classified into two categories: synoptic and climatological analyses based on conventional surface and rawinsonde observations to document the associated dynamical phenomena (e.g., Akiyama 1979; Ninomiya 1984; Tao and Chen 1987) and analyses using remote sensing techniques including satellite and

Corresponding author address: Dr. Jian-Jian Wang, Mesoscale Atmospheric Processes Branch, NASA Goddard Space Flight Center, Greenbelt, MD 20771.
E-mail: jjwang@agnes.gsfc.nasa.gov

radar observations to investigate the cloud-physical and kinematic aspects (e.g., Akiyama 1984; Fukao et al. 1988).

Although the heavy rainfall in mei-yu/baiu season usually occurs in June and July, the summer monsoon rainfall in east Asia starts about a month earlier in the Indochina and South China Sea (SCS) area (Tao and Chen 1987). This summer monsoon region including the SCS and surrounding landmasses is referred to as the southeast Asian monsoon (SEAM). Better understanding of the characteristics of the rainfall evolution and structure in the early monsoon season will extend our knowledge of the formation and maintenance of heavy rainfall events during the monsoon season. Nevertheless, compared to the numerous studies focusing on planetary-scale phenomena and mei-yu and baiu fronts in the mid to late stages of the SEAM, little attention has been given to mesoscale aspects of precipitating systems during its onset (transient) period. The organization and evolution of convection is of considerable interest because it lies at the heart of heat, moisture, and momentum fluxes. It is also believed to be a zeroth-order problem that must be understood before appropriate parameterizations can be developed for use with global models.

The structure and evolution of the tropical convection has been studied for decades by many investigators (e.g., Houze and Cheng 1977; Jorgenson and LeMone 1989; Zipser and Lutz 1994). Since a comprehensive dataset is often necessary for detailed analysis of mesoscale convection, most of studies take advantage of field experiments that target specific locations such as the west Pacific (Trier et al. 1996; Jorgenson et al. 1997; Rickenbach and Rutledge 1998), east Atlantic (Zipser 1977; Barnes and Sieckman 1984), and Maritime Continent (Rutledge et al. 1992; Williams et al. 1992). Conversely, systematic studies on the mesoscale convection in the summer Asian monsoon region are quite rare. A notable contribution to this topic is the work related to the summer Monsoon Experiment (MONEX, 1978–79; Fein and Kuettner 1980). Although MONEX was designed primarily to document large-scale aspects of monsoons, it provided an opportunity to investigate the internal structure of mesoscale convection. With limited radar observations, Smith and Lin (1984) developed an analytical model for flow over a mountain barrier, which caused cumulus development over the west coast of India with an offshore extension of at least 30 km. Grossman and Durran (1984) carried out a more detailed study to explain the rainfall maximum farther offshore.

The Australian Monsoon Experiment (AMEX, 1986–87; Holland et al. 1986) also investigated some aspects related to the Asian monsoon. It was found that the structure and evolution of north Australian cloud lines were closely related to the characteristics of the environmental airflow in the monsoon season (Drosdowsky et al. 1989). During the first half of AMEX Phase I, summer monsoonal westerly flow prevailed in the low
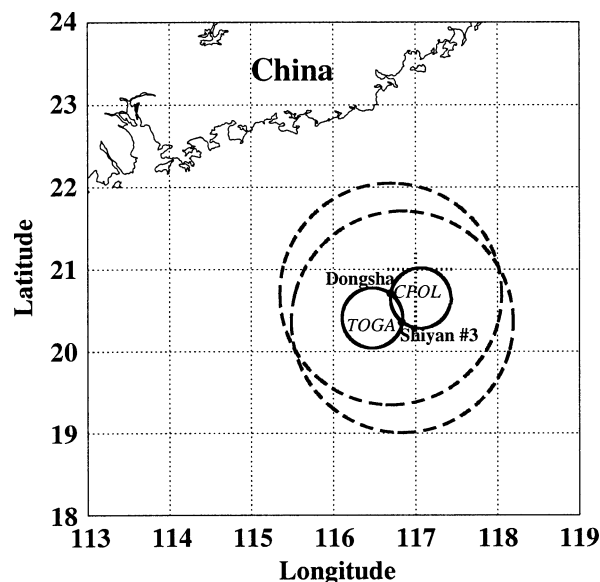

FIG. 1. Dual-Doppler radar network over the South China Sea during SCSMEX. The big dashed circles indicate the radar-observing domain, while the small solid circles show the dual-Doppler radar analysis regime.

levels, and the region experienced more extensive deep convection. Tropical squall lines consisting of a sharp leading edge of deep convective cells and a trailing mesoscale stratiform anvil were observed. After the reestablishment of winter monsoonal easterly flow at the low level in the second half of AMEX Phase I, long thin cloud lines, generally including a series of small cumuli, often occurred. As the easterly flow strengthened and extended farther, the lines became more intense.

With focus mainly on the Arabian Sea, Bay of Bengal, and northern Australian regions, neither MONEX nor AMEX could explore the east Asian monsoon. Although the Asian summer monsoon starts from the onset of SEAM, the SCS area was the last area in the Asian monsoon region without systematic observation and research. As traditional observational networks are far from being adequate, the lack of detailed observations became a significant obstacle to the research on SEAM and related physical processes. The South China Sea Monsoon Experiment (SCSMEX; Lau et al. 2000) was an international field experiment conducted in SCS and surrounding areas during May–June 1998. The goal of the mesoscale program was to define the initiation, structure, evolution, and dynamics of precipitation processes associated with the onset and mature phase of the SEAM. To accomplish this objective, two Doppler radars were deployed to form a dual-Doppler radar analysis region (Fig. 1) in the northern SCS. Other conventional meteorological observational platforms including rawinsonde, surface observation network, and rain gauges were also collocated at the radar sites and surrounding areas. These observations allowed for the

collection of a comprehensive dataset to describe the environment, evolution, rainfall characteristics, and kinematic structure of the monsoon convective systems.

In this paper, the evolution and structure of mesoscale convection observed by SCSMEX dual-Doppler radar network on 15 May 1998 are studied. Unlike previous studies of heavy rainfall events accompanying the quasi-stationary mei-yu/baiu fronts in the mature phase of the summer Asian monsoon, this study focuses, for the first time, on the mesoscale convection associated with a front passage during the onset period of SEAM. The interaction between the tropical monsoon flow and the frontal circulation and the role of such interaction on the evolution and structure of the mesoscale convection are investigated. The rainfall characteristics and three-dimensional kinematic structure of the pre- and postfrontal convection are also examined in detail.

2. Data analysis

The data used in this study are primarily radar data collected during SCSMEX. During SCSMEX, the National Oceanographic and Atmospheric Administration (NOAA)/Tropical Ocean Global Atmosphere (TOGA) radar and Bureau of Meteorology Research Centre (BMRC; Australia) C-band polarimetric (C-POL) radar were deployed to form a dual-Doppler radar network (Fig. 1). The C-POL radar was installed at Dongsha Island (20.7°N, 116.7°E) and operated on a 24-h basis (with several short breaks) throughout May and June 1998. The TOGA radar was installed on the People's Republic of China *Shiyan 3* research vessel (about 20.4°N, 116.8°E) and operated continuously during the two intensive observing periods (IOPs; 5–25 May and 5–25 June). The length of the radar baseline was about 40–45 km, a frequently used range to provide a good areal coverage with reasonable spatial resolution. The typical scanning procedure during SCSMEX involved 10-min 360° surveillance scans at 15 elevations from 0.5° to 30°. Over this period, the target mesoscale system studied was assumed stationary. Additional sources of information on larger-scale background include synoptic reanalysis charts from the National Centers for Environmental Prediction (NCEP), *Geosynchronous Meteorological Satellite-5* (*GMS-5*) imagery, sounding network, and automatic weather stations (AWS).

The main approach of the radar data analyses in this study is the traditional "dual-Doppler" synthesis methods. Those polarimetric variables collected by C-POL radar were only used to help the data quality control and corrections for attenuation of the C-band radar data. The C-POL data were processed to eliminate sea clutter using thresholds in the correlation coefficient between horizontally and vertically polarized echo signals (ρ_{HV}) and the total differential phase (Ψ_{dp}) (Ryzhkov and Zrnic 1998). To correct the reflectivity attenuation, and empirical method described by Carey et al. (2000) was adapted. A linear relationship between the observed differential propagation phase (ϕ_{dp}, calculated from Ψ_{dp}), and the propagation-affected Z was derived by the statistical analysis of the C-POL data. The estimated "correction factors" from the above relationship were then used to estimate the attenuation throughout the radar echo volume. For case of 15 May, the derived formula for reflectivity attenuation correction is

$$Z_{corrected} = Z_{measured} + 0.0623\phi_{dp}.$$

During IOP-1 of SCSMEX, the radar operation groups at Dongsha Island and *Shiyan 3* noticed that the reflectivity data from TOGA were much lower than that from C-POL. The C-POL operation group did several careful calibrations before and during the experiment and believed that C-POL reflectivity data were very reliable. On the other hand, the TOGA operation group was unable to do a complete calibration because of its broken signal generator. After the experiment, it was determined that TOGA reflectivities were reduced because of a misaligned bandpass filter. To quantify the differences, cross-correlation analyses of the reflectivity fields from both radars were performed. In general, the TOGA reflectivities were about 13–16 dBZ lower than C-POL reflectivities. In an independent intercomparison among TOGA, C-POL, and spaceborne Tropical Rainfall Measuring Mission (TRMM; Kummerow et al. 2000) precipitation radar (PR), E. Anagnostou (2000, personal communication) at the University of Connecticut found that PR's reflectivities were about 12–13 dBZ higher than TOGA, but 1–2 dBZ lower than C-POL. Although there is no "truth" in these comparisons, the closer the two measurements were to agreement, the greater the confidence we had. Moreover, in a recent comparison among PR, U.S. Weather Surveillance Radars-1988 Doppler (WSR-88D), and research radars from other TRMM field campaigns, Anagnostou et al. (2001) figured that the main candidate for systematic differences exceeding 1.5 dBZ is the ground radar system calibration bias. Based on these results, it was determined that the reflectivity data from C-POL were much more reliable than those from TOGA. As a result, only the reflectivity data from C-POL were used in this study. An intercomparison of radial velocity fields from the two radars was also done in an area near the baseline. The results showed that the radial velocity fields matched each other very well.

Radial velocity data were manually unfolded using the National Center for Atmospheric Research (NCAR) Research Data Support System (RDSS) software (Oye and Carbone 1981). The C-POL radar reflectivity and radial velocity fields were then interpolated to a Cartesian grid using the NCAR REORDER software (Mohr et al. 1986). Three-dimensional kinematic fields were obtained by synthesizing the radial velocity measurements from the two radars within the analysis domain using NCAR Custom Editing and Display of Reduced Information in Cartesian Space program (CEDRIC; Mohr et al. 1986). With a 40–45-km-long baseline, a

30° intersection angle between beams of the radar, required by a good quality dual-Doppler radar analysis (Davies-Jones 1979), extended out to about 75 km from the baseline. The dual-Doppler radar analysis domain (shown in Fig. 1) was approximately a 150 km × 100 km area extending 15 km in the vertical. The wide beamwidth of TOGA radar (1.55°) compared to C-POL (1.0°) resulted in a coarser resolution in dual-Doppler analysis. In our dual-Doppler radar analysis, the horizontal grid spacing was 1.5 km, and the vertical grid spacing was 0.75 km. The radial velocity analysis was advected to a common time, generally close to the middle of each volume.

Vertical air motion was calculated from the divergence field at each level using the anelastic continuity equation and the upward integration method. The upward integration method was required mainly because of the poor sensitivity of TOGA radar in the upper levels with weak reflectivity. In fact, the 13–16-dBZ low bias from TOGA reflectivity not only underestimated the reflectivity, but also resulted in incomplete data coverage in the areas with weak echoes because the noise threshold was performed at a much higher level than expected. The incomplete data sample at the top levels made it difficult to defining the upper-boundary condition. Without the establishment of upper-boundary conditions, variational and downward integration are impossible and the estimation of vertical velocity using upward integration in this study is subject to some uncertainty. The analysis process outlined in Wakimoto et al. (1998, their appendix) was adapted to estimate the error from upward integration. Assuming that the standard deviation of the mean Doppler velocities measured by the two Doppler radars are 1 m s^{-1}, the standard deviation of the vertical velocity for upward integration at 1.5, 4.5, and 9.0 km is about 1.5, 3.3, 6.9 m s^{-1}, respectively. Apparently, the derived vertical velocities are not reliable in the upper regions. There are two options for the presentation of the vertical velocity field: one is to terminate the syntheses at a certain level, for example, 4.5 km; the other is to show the complete field with full awareness of the possible errors at high levels. After careful cross-checking of the derived vertical velocity and the reflectivity fields, it was found that at least the pattern of the vertical velocity matches the pattern of reflectivity very well, even at high levels in most cases. Therefore, to have a better picture of the case study, the derived vertical velocities will be shown in the whole vertical cross sections. However, no conclusion will be made from the derived vertical velocities at high levels.

To filter noise in the vertical velocities, the horizontal wind fields derived from the dual-Doppler solution are lightly smoothed with a two-pass Leise (1981) filter prior to divergence calculation and vertical integration. This procedure significantly damps wavelengths up to 6.0 km and removes wavelengths of less than 4.5 km. The storm motion vector was calculated by inspection

of the leading edge of the convection in a sequential horizontal cross section of low-level reflectivity.

3. Synoptic conditions

Prior to 15 May 1998, the SCS region was mainly under the control of the subtropical high over the western Pacific (Ding and Liu 2001). On the western flank of the subtropical high, low-level airflow at 850 hPa exhibited southeasterly winds in the southern SCS and southwesterly winds in the northern SCS (Fig. 2a). At the 200-hPa level, there was an anticyclone located in the Bay of Bengal (Fig. 2b). Under its influence, northerly flow was observed over the SCS. NCEP reanalysis revealed low-level divergence and upper-level convergence over the SCS (Figs. 2a and 2b, respectively), providing an unfavorable condition for the development of convection. From the beginning of IOP-1 on 5 May, frontal passages from northwestern China to the coastal regions were observed periodically with an interval of 2–4 days. The well-developed frontal cloud/rainbands usually extended from south China along the coast to the Korean peninsula and Japan. An example of this type of frontal cloud band on 11 May is shown in Fig. 3a. However, once the southern part of the frontal cloud band passed the China coast into the northern SCS, the cloud/rainbands associated with the front weakened and dissipated (Fig. 3b).

The large-scale wind fields started to change, especially at low levels, in the northern SCS on 15 May. At 850 hPa, compared to the wind field days before, the western Pacific subtropical high had retreated eastward (Johnson and Ciesielski 2002) and a cyclonic system had developed in eastern China. More importantly, there were two more branches of airflow joining the existing southwesterly flow. The first branch originated in the Bay of Bengal to the east of the equatorial twin cyclone (only the northern cyclone centered near 10°N and 82°E shown in Fig. 2c). The second branch was the cross-equatorial airflow, originating in the Australian region in the Southern Hemisphere. These two airflows are the main components forming the east Asian summer monsoon (Tao and Chen 1987). The merging of equatorial flows into the northern SCS region also resulted in an increase of relative humidity to over 70% (not shown), a significant mark of the onset of SEAM (Lau et al. 2002). At 200 hPa, the strong anticyclone continuously dominated the Indochina region and the surrounding SCS area to form a diffluent field (Fig. 2d). The wind fields in the SCSMEX domain shifted from low-level divergence (2.5 × 10^{-6} s^{-1}) and upper-level convergence (−20 × 10^{-6} s^{-1}) on 11 May to low-level convergence (−5.0 × 10^{-6} s^{-1}) and upper-level divergence (10 × 10^{-6} s^{-1}) on 15 May (Fig. 2). On 15 May, a pronounced frontal cloud band oriented from southwest to northeast covered most coastal regions of southeastern China (Fig. 3c). Different from the frontal cloud band reaching the coastal region 4 days earlier, this sys-
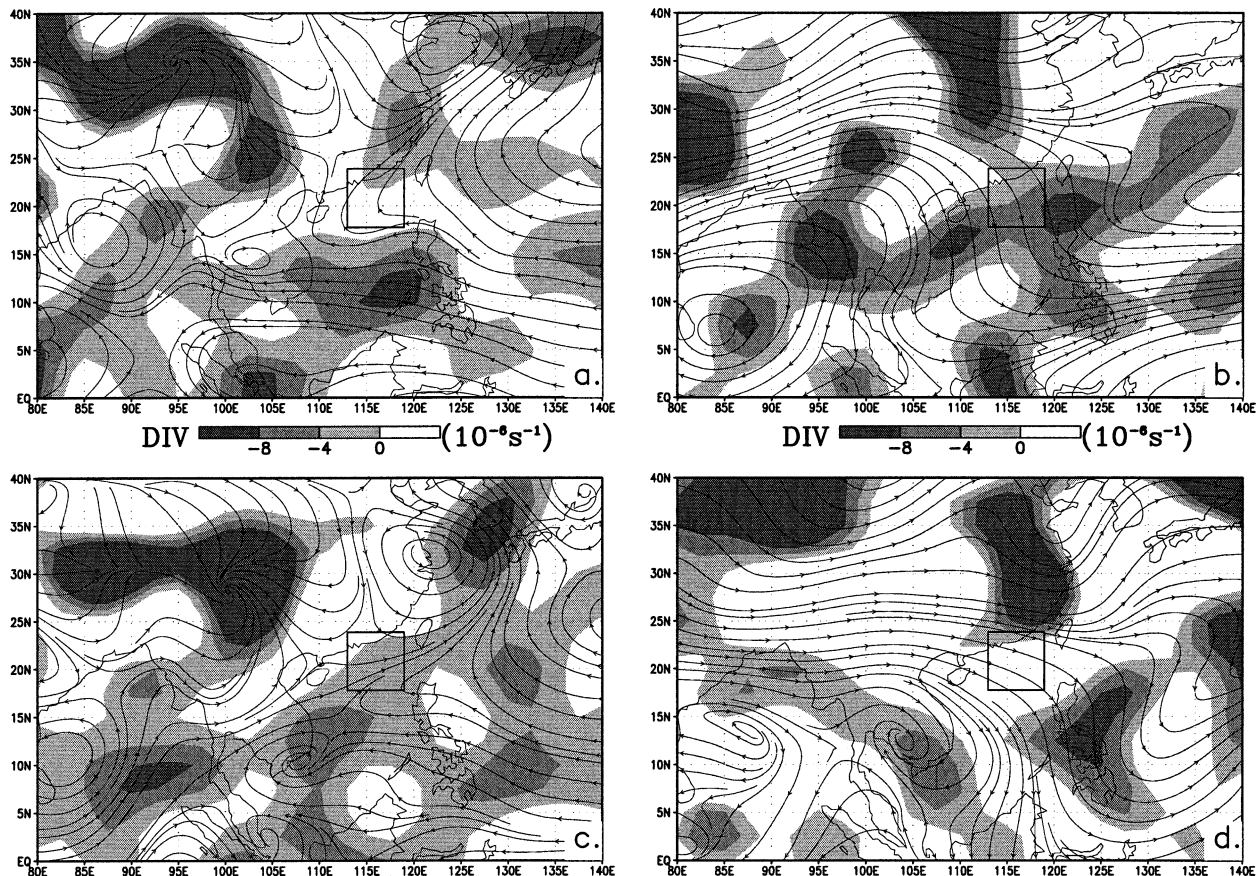
FIG. 2. NCEP constant pressure level reanalysis at (a) 850 hPa, (b) 200 hPa valid at 0000 UTC 11 May, (c) 850 hPa, and (d) 200 hPa valid at 0000 UTC 15 May. The divergence is shaded as shown in the middle of the figure. The squares denote the domain shown in Fig. 1.

tem was able to move into the sea without weakening. In fact, after the start of the summer monsoon onset in the northern SCS, the intensity and areal coverage of the frontal cloud bands even became enhanced in the southern portion (partially over the northern SCS) (Fig. 3d). Similar to the observations during AMEX (Drosdowsky et al. 1989), deep and intense convection in the SCS region also developed in the summer monsoonal westerly regime.

The case of 15 May studied herein was the first intense mesoscale convection observed in the SCS region during SCSMEX and also recorded as the rainiest day at Dongsha Island during IOP-1 with 43-mm precipitation. The AWS data (not shown) indicated that the arrival of the surface cold front in the tropical SCS region, characterized by a mild temperature drop and a quick wind direction shift, occurred at Dongsha Island around 0600 UTC (LST = UTC + 8 h). The prefrontal sounding taken at *Shiyan 3* at 0600 UTC (Fig. 4) showed moderate instability—the convective available potential energy (CAPE) was about 1690 J kg^{-1}. The low-level (surface to 800 hPa) wind shear was westerly with a magnitude of 5.4 m s^{-1} or 2.8×10^{-3} s^{-1}. The lifting condensation level (LCL) was at 938 hPa ($\sim$0.7 km),

while the level of free convection (LFC) was at 847 hPa ($\sim$1.5 km). The postfrontal sounding launched at Dongsha Island at 1200 UTC (Fig. 4) had a deep saturated layer from near surface to about 400 hPa. The postfrontal sounding showed a higher CAPE of 1950 J kg^{-1} along with a lower LCL (1001 hPa) and LFC (973 hPa). The increased CAPE seems to be the result of less stable air coming with the tropical monsoon flow. The main difference of the wind profile from the two soundings was that winds at the lower levels (900–600 hPa) shifted from prefrontal southwesterly to postfrontal northwesterly.

4. The evolution of convection

When discussing mesoscale convection related to a frontal passage, terms of prefrontal and postfrontal precipitation are frequently used for activities before and after the passage of the *surface front*. However, from previous synoptic-scale analysis of east Asian monsoon convection (e.g., Chen and Hui 1992; Ding 1994), we found that the front at 850 hPa, characterized by a wind shear line separating the southwesterly winds ahead of it and northwesterly winds behind it, could be a better
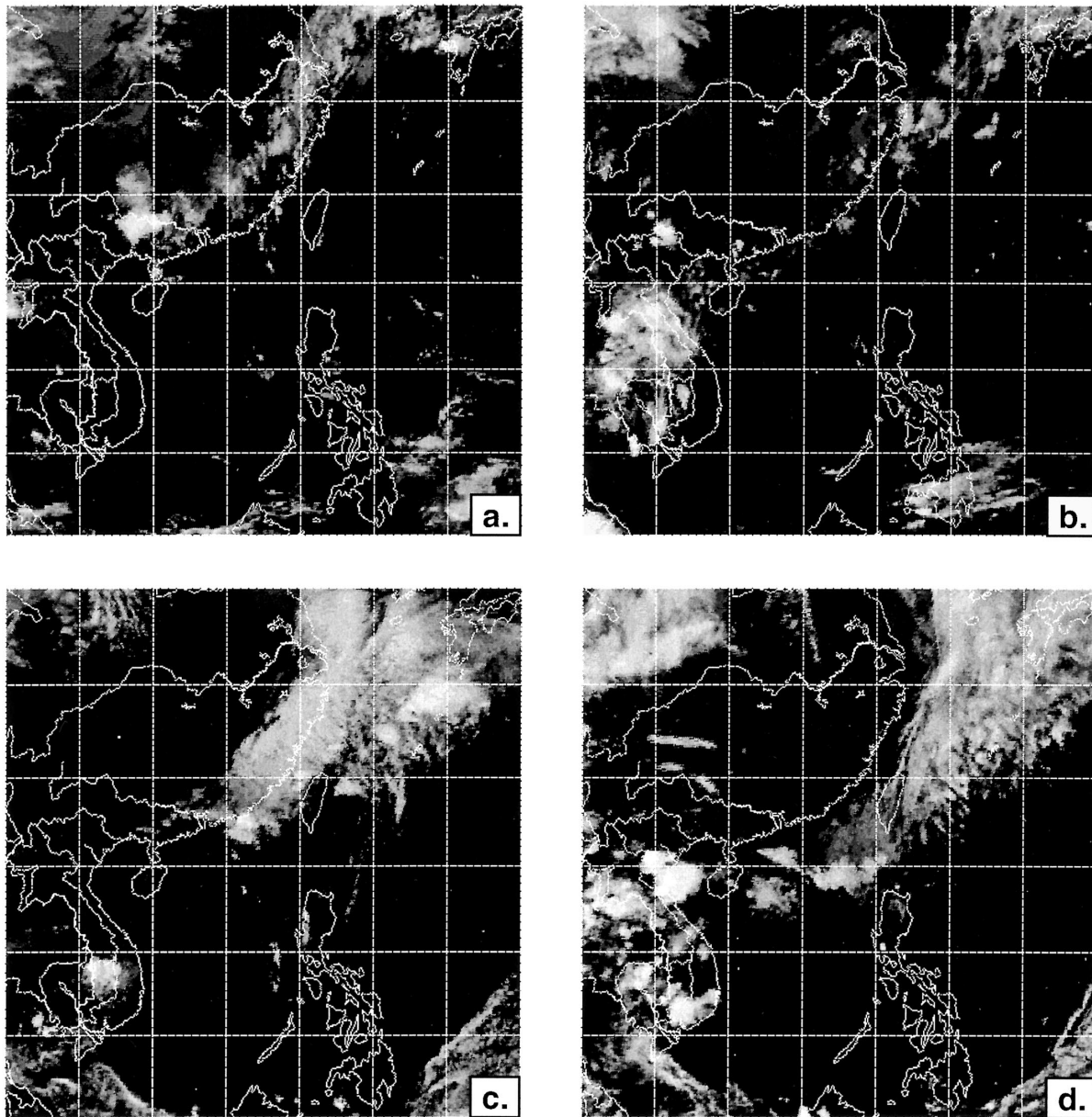
FIG. 3. Infrared imageries from *GMS-5* at (a) 0000 UTC 11 May, (b) 1500 UTC 11 May, (c) 0000 UTC 15 May, and (d) 1200 UTC 15 May.

choice to decide the pre- and postfrontal convection. First, the front at 850 hPa has more dynamic links to the occurrence of deep convection. As the cold air penetrated to the subtropical region, the cold pool behind the surface front was rather shallow with a sharp vertical tilt. The lifting along the leading edge of the shallow cold air alone may not be adequate to initiate convection, and heavy precipitation frequently occurs ahead of the 850-hPa trough (Chen and Hui 1992; Li et al. 1997). The vertical tilt of the front on 15 May was on the order of 1/300 (not shown) similar to that observed during

Taiwan Mesoscale Experiment (TAMEX) (Chen and Hui 1992), compared to a 1/50 to 1/100 vertical tilt of a midlatitude cold front. Second, the front at 850 hPa has more thermodynamic significance on the development of deep convection. The low-level water vapor flux has its maximum near the front at 850 hPa, while most water vapor concentrates in the boundary layer below 850 hPa (Ding 1994). In the present study, the convective characteristics in the pre- and postregion of the front at 850 hPa were quite different although they were both behind the surface front. Hereinafter, discus-
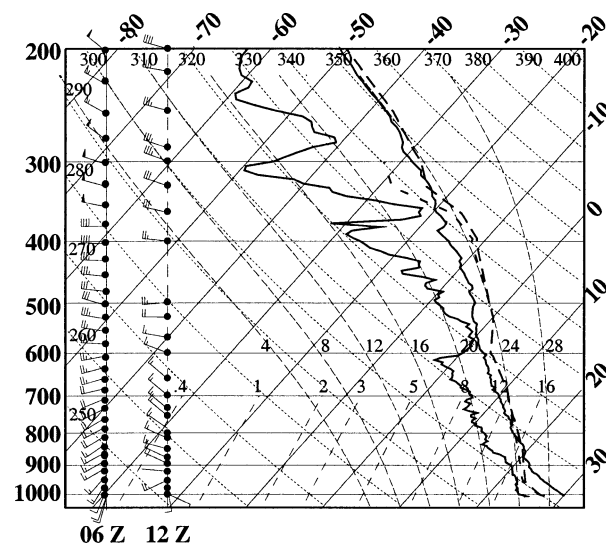
FIG. 4. Sounding launched from research vessel *Shiyan 3* at 0600 UTC (solid lines) and Dongsha Island at 1200 UTC (dashed lines) 15 May 1998.

sion on the evolution and structure of the mesoscale convection will be in the context of its relative position to the front at 850 hPa.

At 0600 UTC, the main feature in the radar domain was the linear northeast-to-southwest-oriented frontal rainband with a width of about 40 km (A in Fig. 5a). This rainband had a maximum radar reflectivity over 50 dBZ and was close to the front at 850 hPa. Ahead of the convective line A, there were two groups of newly formed convection at 50 km east to C-POL. Johnson and Keenan (2001) noted that the convection in the prefrontal region might orient relative to the low-level and/or midlevel wind shear. The convective line ahead of the front (B in Fig. 5a) was oriented north to south (Fig. 6a), while secondary convective lines (B1 and B2 in Fig. 5a) located in the middle of east dual-Doppler lobe were oriented east to west. In their studies on western Pacific convection, LeMone et al. (1998) found the orientation of the convection tends to be perpendicular to the low-level wind shear if its magnitude is over 4 m s^{-1}. They also noted that the secondary lines were
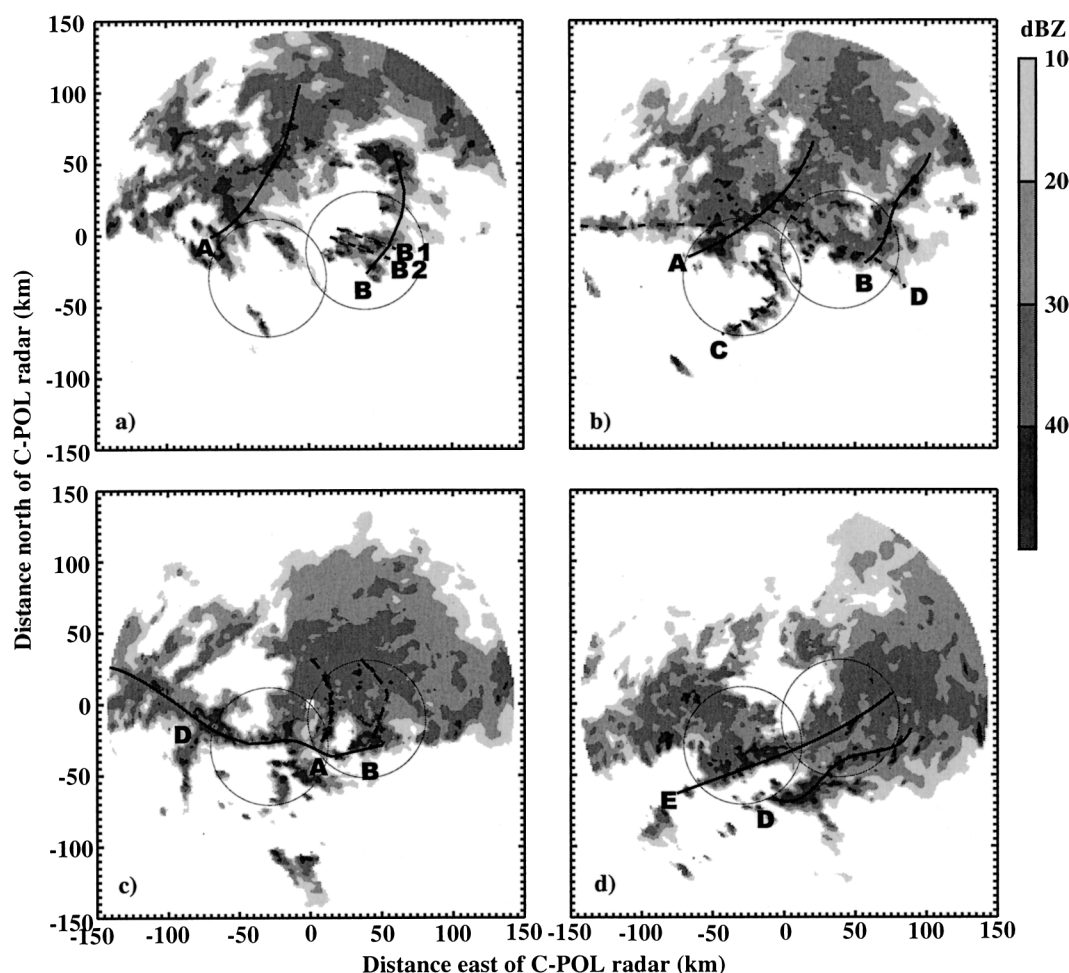

FIG. 5. C-POL radar reflectivity (dBZ) at 2.5 km MSL at (a) 0600, (b) 0700, (c) 0830, and (d) 0930 UTC 15 May 1998.
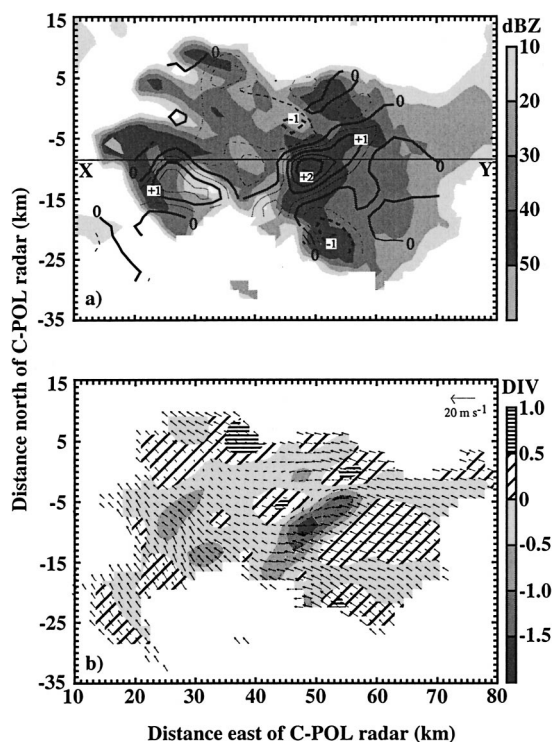
FIG. 6. (a) Radar reflectivity (dBZ) and vertical air motion contoured at an interval of 0.5 m s^{-1} and (b) system-relative wind flow and divergence (10^{-3} s^{-1}) at 1.5 km MSL valid at 0620 UTC. The 20 m s^{-1} scaling vector for winds is shown to the upper-right-hand corner of (b).

parallel to the low-level shear. On 15 May, the low-level vertical wind shear in the prefrontal region is westerly with the magnitude of 5.4 m s^{-1} (Fig. 4). The orientation of convective lines was consistent with the conclusion made by LeMone et al. The convection had a larger areal coverage an hour later at 0700 UTC (Fig. 5b). Meanwhile, between the two northeast-to-southwest-oriented convective lines and beyond, there was a tendency to form a narrow convective line (D in Fig. 5b) perpendicular to the earlier convective lines. This new line intensified and became the primary feature in the following hours. Another feature at 0700 UTC was the new developing convective line (C in Fig. 5b) in the prefrontal region with low-level southwesterly winds prevailing (not shown). The development and structure of this convective line were very similar to the early formed prefrontal convection (B in Fig. 5) that will be analyzed in detail in section 5.

From continuous dual-Doppler analysis of wind fields, it was found that the front at 850 hPa separating the prefrontal southerly and the postfrontal northerly winds passed the C-POL at about 0730 UTC (not shown). In the next hour, the orientation of the main convective line exhibited a dramatic change. As shown in Fig. 5c, the main radar echo became an east–west-oriented convective line across the dual-Doppler radar analysis region. This was the convective line that had

started to form at 0700 UTC (Fig. 5b) in the postfrontal region. The primarily northeast-to-southwest-oriented convective lines dominant in earlier hours weakened during the same period. The area with radar reflectivity over 40 dBZ reduced remarkably. Two weak north–south-oriented lines existed to the north of main convection as the residual from the early convection. A large area of stratiform precipitation of the prefrontal convection was also observed in the northeast quadrant. During SCSMEX, this type of sharp change of convective orientation in a time period of several hours was also frequently observed in other cases. At 0930 UTC, the north-to-south-oriented convective lines continued to dissipate with some stratiform precipitation remaining. On the other hand, the primary east-to-west-oriented convective lines became more pronounced, showing increased areal coverage and enhanced intensity (Fig. 5d).

5. The structure of convection

For case of 15 May, we have performed 5-h of dual-Doppler radar analysis from 0600 to 1100 UTC when the frontal convection was in the dual-Doppler analysis lobes. After carefully examining over 60 continuous radar volumes from both C-POL and TOGA radar, we are able to study the development and evolution of every convective band in detail. The representative horizontal and vertical cross sections are selected and presented in this section to illustrate the horizontal and vertical structure of the pre- and postfrontal convection at their mature phase.

a. Prefrontal convection

The convection that was ideally located in the dual-Doppler radar analysis lobe about 15–70 km east of C-POL (B in Fig. 5a) was chosen as a representative of the prefrontal convection. The system-relative wind fields at 1.5 km MSL (Fig. 6b) show that low-level inflow was from front (southeast) to rear (northwest). The system-relative wind inflow speed ahead of the convective lines was about 6–7 m s^{-1}. The deceleration of the relative southeasterly inflow ahead of the convective line caused a northeast-to-southwest band of low-level convergence up to 1.8×10^{-3} s^{-1}. A cellular updraft zone corresponding to the strong low-level convergence was located in the central portion of the reflectivity maxima, with a maximum vertical speed over 2.0 m s^{-1} (Fig. 6a). This updraft zone resulting from the convergence of the southerly flow was the key to maintain the intensity of the convection. To the northwest of (behind) the convective core, a narrow band of divergent flow and descending flow was found matching the minimum reflectivity of 15–25 dBZ (Fig. 6). The downdraft followed updraft likely as a result of a pressure deficit in the low levels induced hydrostatically by the rearward spreading of warm and moist air from the updraft dy-
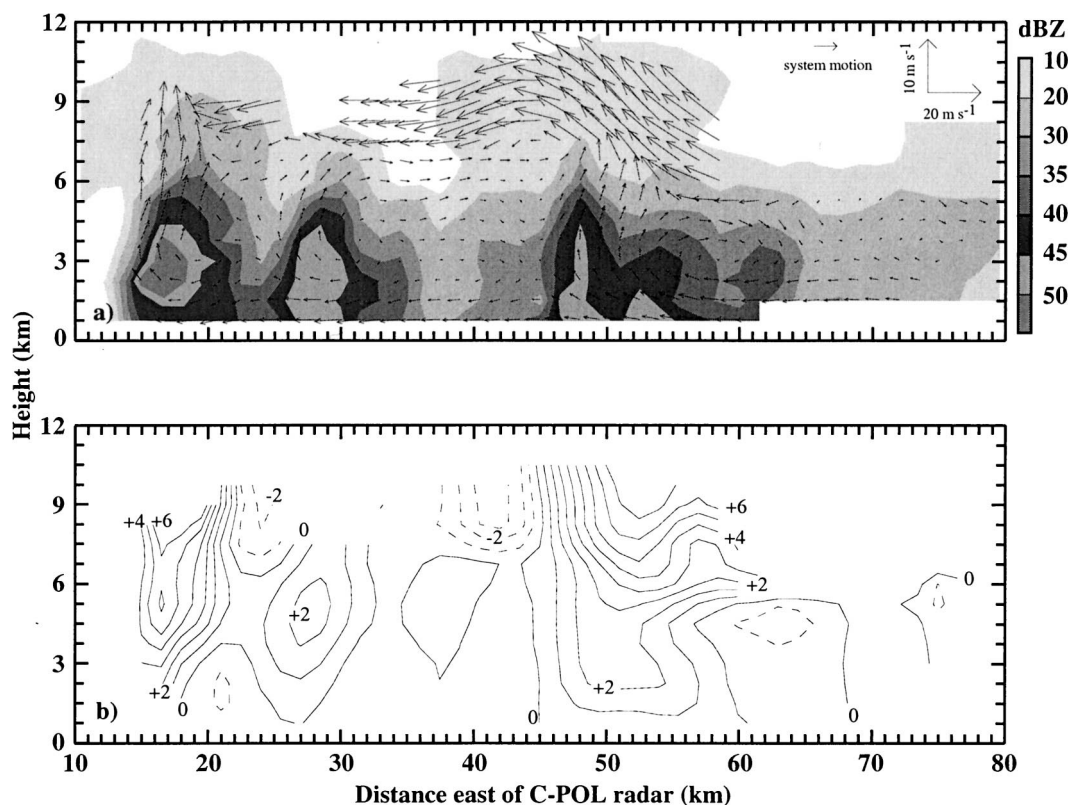
FIG. 7. Vertical cross section of (a) reflectivity and line-normal system-relative wind and (b) vertical air motion contoured at an interval of 1 m s^{-1} along XY in Fig. 7 valid at 0620 UTC.

namically by the interaction of the updraft and the ambient wind shear (Weisman 1992). Meanwhile, the downward motion following the updraft center and reflectivity maxima indicated a descending front-to-rear flow (Rotunno and Klemp 1982). Ahead of the reflectivity maximum, there was an area of weak subsidence associated with the weak divergent flow. As addressed in section 2, because of the low sensitivity of TOGA radar, many useful data at upper levels were lost when the reflectivity was weak. This restricted the ability to do quality dual-Doppler radar analysis at upper levels. Therefore, no upper-level horizontal cross section is discussed.

A vertical cross section through the convective complex (Fig. 7) is made to characterize the structure of airflow and vertical circulation. The echo top, denoted by 10-dBZ reflectivity isopleth, was at about 11 km MSL. Compared to the typical rearward sloping structure observed in the tropical convection (e.g., Jorgenson et al. 1997), a notable characteristic of this convection was that the reflectivity pattern was almost straight upward without much slope. When downshear tilting updraft usually occurred in an environment with strong vertical wind shear (Rotunno et al. 1988), the convection with little tilt as shown in Fig. 7 was often found in an environment without strong vertical wind shear (Fig. 4). During the summer monsoon onset period in 1998, the

westerly winds generally dominated through the whole convective layer as the onset of upper-level northwesterly winds occurred at the end of transition. As a result of limited vertical wind shear, the straight upward echo pattern with little tilt was commonly observed during the period. The front-to-rear low-level inflow started from the lowest level with the maximum strength below 1.5 km MSL. The maximum low-level convergence and updraft were located in the rear part of the convection (45–50 km east of C-POL) about 20–30 km behind the leading edge (70–75 km east of C-POL; Fig. 7b). This is different from other tropical convective lines previously studied (LeMone et al. 1984; Jorgenson et al. 1997), which often have a maximum low-level convergence and updraft in a narrow ribbon within 1–2 km of the leading edge. Numerous studies have emphasized the important role played by the cold pool and the convective downdraft in the maintenance of the convection (e.g., Wakimoto 1982). The evaporative cooling of raindrops results in cool air brought down to the surface in the form of convective downdrafts. Downdrafts spread at the ground and carry some of the momentum from middle levels, thereby enhancing the convergence at the outflow boundary. For those tropical convections with maximum updraft at the leading edge, the systematic downdraft was located immediately following the leading edge. However, in a straight upward cell with little

tilt (Fig. 6a), the potential downdraft near the leading edge would encounter the low-level inflow and updraft. While the downdraft was usually weaker than the updraft in the convective core (LeMone and Zipser 1980), the downdraft was only found farther behind, about 7–10 km from the reflectivity maxima (Figs. 6 and 7) where the updraft was weak. In addition, this structure also implies that inflow must pass a raining area ahead of the convective core before entering the convective towers. From a simple 2D numerical simulation, Parker (2002) argued that the evaporative cooling actually occurs over a relatively deep layer, with cooling increasing with height over the lowest 2–2.5 km. Therefore, the net effect of this process is to further destabilize the low levels and result in an increased CAPE. Thus, the cooling of inflow parcels ahead of the convective core did not appear to be a detriment to long-lived systems. In addition, Parker and Johnson (2001) noted that strong lifting along the edge of the cold surface outflow (i.e., the front) might also be helpful to bring the air parcel to the level of free convection. The updraft was mainly located just east of the reflectivity maxima (Fig. 7b) at a maximum speed of 6.7 m s^{-1}. This moderate updraft was comparable to most tropical convection (Zipser and LeMone 1980; Jorgenson and LeMone 1989).

Ahead of the convective cells, system-relative westerly rear-to-front flow was observed at the midlevels (e.g., 4.5 km MSL), blowing the particles ahead of the line (Fig. 7a). In most tropical convection, the stratiform rains were found behind their convective counterpart (trailing mode) as a result of the mid- to upper-level outflow in the same direction as low-level inflow (Jorgenson et al. 1997; Protat and Lemaitre 2001). However, the prefrontal convection studied here had a tendency to form the stratiform rain ahead of the convective rain (leading mode; Figs. 6a and 7a) in response to the forward advection of hydrometers. In a climatological study, Parker and Johnson (2000) found that the trailing or paralleling stratiform rain occurs in over 80% of convective lines observed in the midlatitudes over the United States, while the leading stratiform cases only account for 19%. However, during the onset of SEAM, leading stratiform rain occurred quite often. In addition to the case of 15 May, there were other convective cases (e.g., 24 May) showing similar structure (Wang 2001). At the upper levels, strong easterly system-relative winds dominated over the convective core (Fig. 7a). Compared to the prefrontal sounding (Fig. 4), these high-level easterly winds were purely convection driven as described in a two-dimensional theoretical model by Moncrieff (1992).

Interestingly, with such strong system-relative easterly winds, the radar echoes at the upper levels were limited in a small area. The hydrometers were concentrated over the top of the intense convective core, but lacked an extension to the downwind side. The environmental conditions before the arrival of the front showed a very dry layer at 300 hPa (~9 km MSL; Fig.

4). The dry air in the upper levels might result in a quick evaporation and sublimation of the forming stratiform cloud when the hydrometers were quickly blown from the top of the convection. The moistering at the upper levels due to the evaporation and sublimation of the hydrometers was also evident from the postfrontal sounding collected at 1200 UTC at Dongsha Island (Fig. 4) which exhibited a much moister upper layer compared to 6 h earlier.

b. Postfrontal convection

The prefrontal convection observed in the radar domain weakened after the passage of the front at 850 hPa. At 0830 UTC, the remaining stratiform rainfall from prefrontal convection covered most of the northeast quadrant (Fig. 5c). The new east-to-west-oriented convection that formed after 0700 UTC in the postfrontal region became the most active convection in the region. At 0930 UTC, the dominant features were two intense east-to-west-oriented convective lines (D and E in Fig. 5d). The most pronounced change of postfrontal convection from prefrontal convection was the sharp orientation change along with the considerable intensification of convection (Fig. 8a). Compared to prefrontal convection, the postfrontal convection had a much larger area of strong convection (reflectivity over 40 dBZ) along with several convective cores showing maximum reflectivity of 55 dBZ.

After the front passage, the northerly flow behind the front prevailed at lower levels in the large northern domain, while the southerly flow from the tropical region accompanying the monsoon onset was present in the small southern domain (Fig. 8b). Contrasting to the prefrontal convection resulting from the convergence of several branches of southerly flows, the enhancement and maintenance of the postfrontal convection were related to the convergence generated from the postfrontal northerly flow from midlatitudes and the southerly monsoon flow from the Tropics. At 1.5 km MSL, a nearly east–west-oriented wind shear line separating the system-relative southeasterly flow from south and the system-relative northeasterly flow from north was observed at the leading (southern) edge of the radar echo (Fig. 8b). As a result, a low-level convergence zone with the maximum magnitude up to 3.0×10^{-3} s^{-1} was located near the leading edge of the convective line. The postfrontal low-level convergence generated by two airflows in the opposite direction was much stronger than that of the prefrontal area with two branches of flows in almost the same direction. The maximum updraft associated with the postfrontal convergence at 1.5 km MSL was up to 3.1 m s^{-1}. It is noted that the convective line and the low-level convergence zone had little movement in the north–south direction. This quasi-stationary convective line was caused by the persistent low-level convergence resulting from the interaction of southerly tropical monsoon airflow and the northerly midlatitude
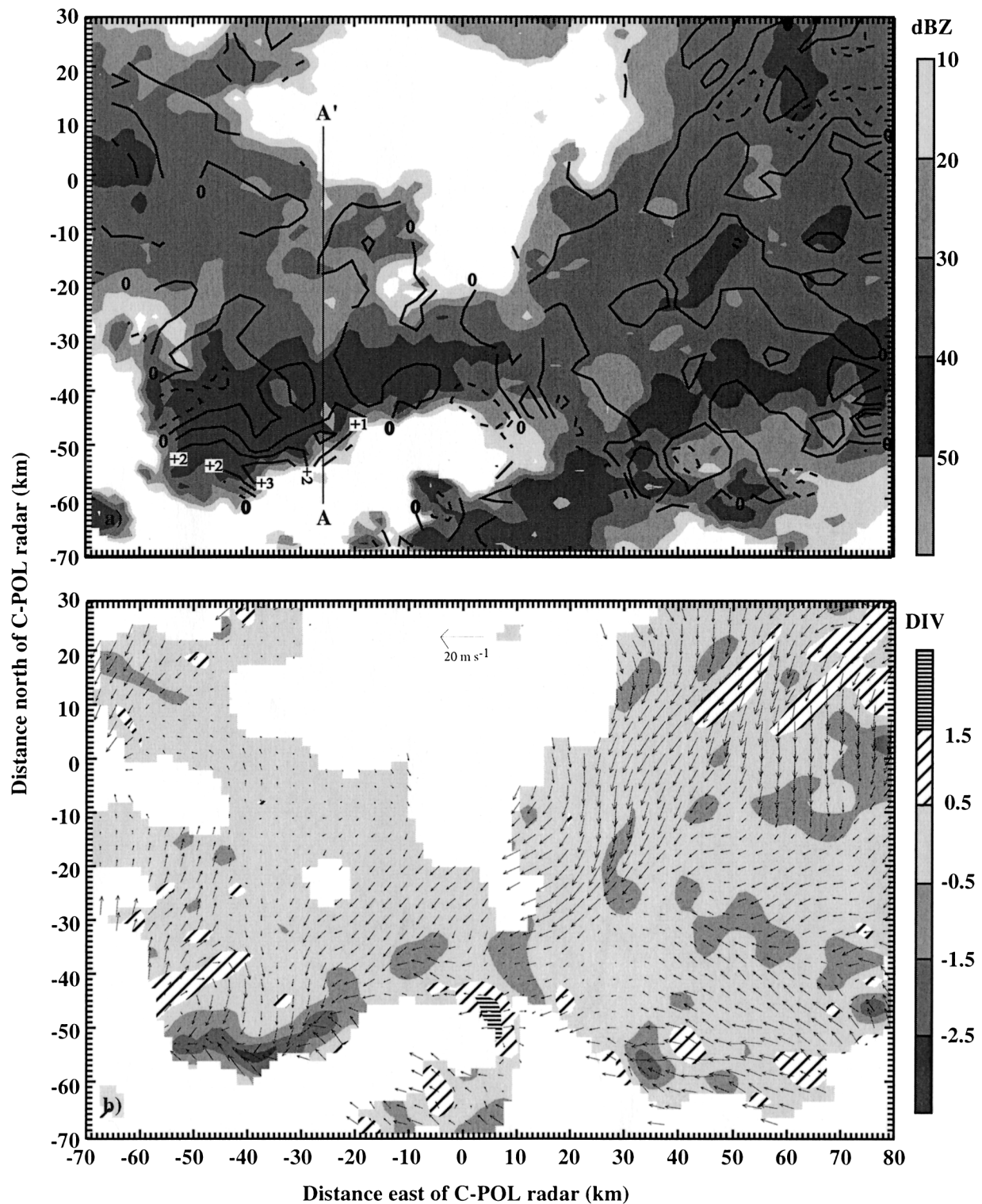
FIG. 8. Same as Fig. 6, except valid at 0930 UTC, and vertical air motion is contoured at an interval of 1 m s^{-1}.
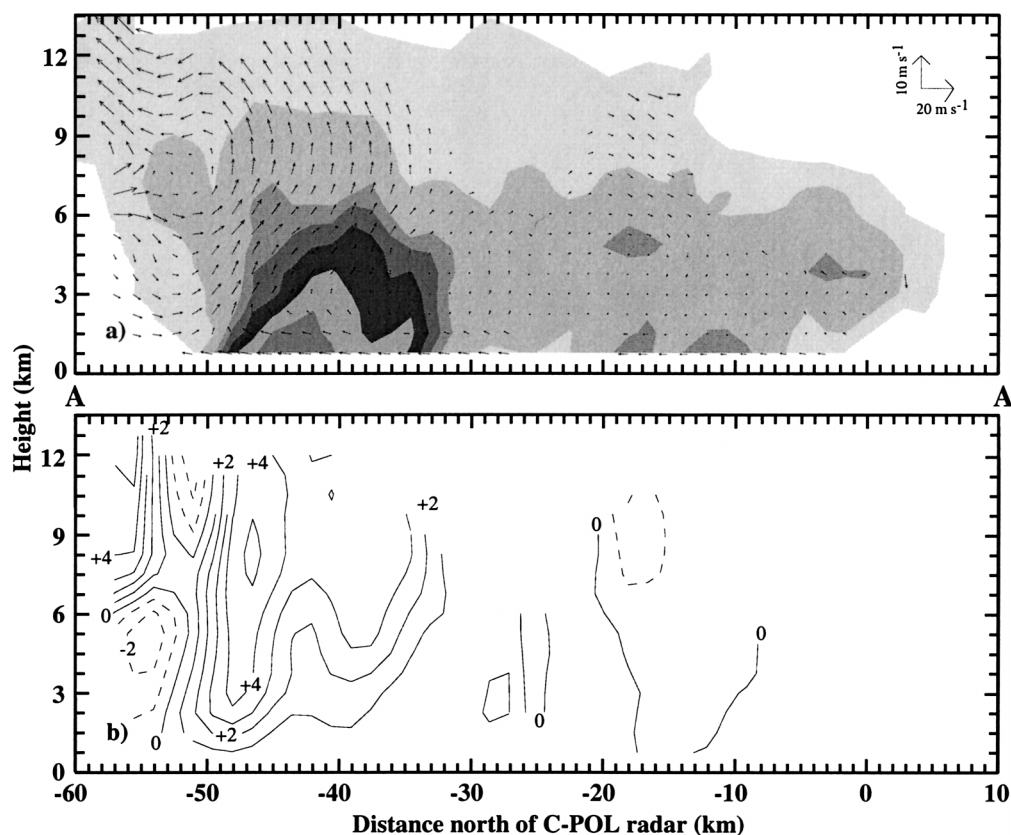
FIG. 9. Same as Fig. 7, except along AA′ in Fig. 8 and valid at 0930 UTC.

airflow. The forming and maintenance of this stable east–west-oriented convective line, though during a relatively short period, was very similar to that of the mei-yu/baiu frontal rainfall affecting mainland China and Japan since June as a result of the interaction between the air mass from the midlatitudes and the tropical airflow from the lower latitudes.

Compared to the prefrontal convection (Fig. 7), the postfrontal convection was taller and more intense (Fig. 9). The maximum reflectivity was over 55 dBZ, with an echo top surpassing 13 km MSL. The similar contrast between the pre- and postfrontal convection was also found in other cases associated with a frontal passage, for example, cases of 17 and 19 May, during the period of summer monsoon onset. The contrast in convective intensity could be related to a much stronger low-level convergence and updraft in the postfrontal region than that in the prefrontal area (Figs. 6 and 8). It is also noticed that the postfrontal sounding at 1200 UTC showed a higher CAPE and more instability than the prefrontal sounding at 0600 UTC (Fig. 4). This could be a result of more tropical airflows coming to the region associated with the onset of the summer monsoon. The higher CAPE and more instability may also contribute to a more intense postfrontal convection as well. The structure of the postfrontal convection (Fig. 9) contains some common characteristics of tropical convection.

The low-level inflow was from the warm and moist tropical air ahead of the leading edge. With the maximum low-level convergence near the narrow leading edge of the convective line, the center of the updraft was in front of the convective core. There was a rapid reflectivity reduction with height above the melting level (~4.5 km MSL) as a result of relatively weak updraft velocities in the Tropics (Zipser and LeMone 1980). The maximum updraft velocity was recorded over the convective core at an elevated height (7.5 km MSL) with a magnitude of 5.5 m s^{-1} (Fig. 9b). However, departures from the typical tropical convection were also evident. The upward inflow did not go through to the rear part at the upper levels. Instead, it turned to a rear-to-front flow above 7.5 km MSL. As a result, a stratiform echo formed at upper levels ahead of the convective line resulting from the frontward advection of hydrometers contributed by the relative flow across the leading edge. While both the prefrontal and postfrontal convection exhibited a formation of leading stratiform region ahead of the convective counterpart, there was different kinematic structure behind them. In the prefrontal convection, the stratiform rain up-front was caused by the midlevel rear-to-front flow. Although strong front-to-rear flow dominated at upper levels in prefrontal convection, the dry environmental air near 300 hPa at 0600 UTC (Fig. 4) prevented the stratiform rain from forming

FIG. 10. CFADs and mean profiles of radar reflectivity, system-relative u and v components, and divergence at (left) 0620 and (right) 0930 UTC 15 May. Bin size is 4 dBZ for reflectivity, 1 m s^{-1} for u and v components, and 1×10^{-3} s^{-1} for divergence. Note the change in scale in the divergence CFADs and mean profiles.

in the trailing area. In the postfrontal convection, the leading stratiform rain was caused by strong rear-to-front upper-level outflow.

Following the 20–30-km-wide convective area was an area of minimum reflectivity with descending airflow in the region. Farther north (right-hand side of Fig. 9)

was a patch of stratiform rain. This stratiform rain was not the trailing part from the convective portion but was the residual from the earlier convection. A brightband structure (~4.5 km MSL; Fig. 9a) in the reflectivity data was located at and below the melting layer. In most stratiform regions, mesoscale updraft exists above the

bright band while mesoscale downdraft is present below the bright band (e.g., Biggerstaff and Houze 1991). However, at the time shown here, the descending flow existed throughout the whole layer of the stratiform region. This was consistent with the fact that the stratiform rain was from decaying convection rather than the dynamically active trailing stratiform echo. A much lower echo top in the stratiform region than that in the convective region (Fig. 9a) provided more evidence for the existence of descending flow at mid- to upper levels.

c. Statistical vertical structure

The contoured frequency by altitude diagrams (CFADs; Yuter and Houze 1995) is a convenient tool for displaying multiple histograms in a two-dimensional format. The relative frequency of occurrence of a given parameter can be shown at each height. To study and compare the vertical structure of the prefrontal and postfrontal convection, we examine mean profiles and CFADs of reflectivity, system-relative u component (eastward) and v component (northward), and divergence at 0620 and 0930 UTC (Fig. 10). At the lowest level, the occurrence of reflectivity over 30 dBZ was identical at 0620 and 0930 UTC (Figs. 10a and 10b). However, from 0.75 to 5 km MSL, both the mean profile and the 10% contour show that the reflectivity at 0620 UTC had a much higher decrease rate with the increase of height. At 5 km MSL, the mean profile of radar reflectivity dropped to slightly over 30 dBZ at 0620 UTC, but reached near 40 dBZ at 0930 UTC. At upper levels, the convection at 0930 UTC also had a significantly higher frequency of occurrence of intense echo features. The probability of occurrence of 30-dBZ echo fell below 10% at about 9.5 km MSL at 0930 UTC compared to 7 km MSL at 0620 UTC. DeMott and Rutledge (1998) suggested that the rainfall production is larger for radar echoes with higher maximum 30-dBZ echo heights. Therefore, it was likely that the postfrontal convection would produce higher rain rates. Overall, the convective activity at 0930 was taller with more intensity than that at 0620 UTC. We have compared the results from this study to the median vertical profiles of radar reflectivity of convective cells in the Global Atmospheric Research Program (GARP) Atlantic Tropical Experiment (GATE) and with the top 10% of convective cells from TAMEX (Zipser and Lutz 1994) and found that the variation of radar reflectivity with height at 0930 UTC was very similar to the previous studies.

The system-relative u component was negative at the lowest levels at both 0620 and 0930 UTC (Figs. 10c). For the north–south-oriented and eastward moving prefrontal convection, it indicated the front-to-rear low-level inflows. Not surprisingly, the system-relative v component was at the opposite sign at the low levels in the pre- and postfrontal regions (Figs. 10e and 10f). The southerly winds controlled the low levels at 0620 UTC, and the northerly winds dominated the low levels

at 0930 UTC. At both times, the mean system-relative u and v components were weak at midlevel (4–6 km MSL), showing a system propagation speed close to the midlevel winds. The apparent differences between the system-relative flows were found at levels above 6 km MSL, especially at high levels ($\sim$10 km MSL), for the prefrontal and postfrontal convection. At 0620 UTC, strong front-to-rear outflow was evident with the high probability of occurrence of negative relative u component. The mean system-relative v component exhibited strong convective-driven southerly winds at the levels over 7 km MSL (refer to the prefrontal sounding in Fig. 4). At 0930 UTC, the mean profile of the u component at the upper level oscillated around 0. Weak rear-to-front flows had the highest probability of the occurrence, while a small portion of front-to-rear flows also existed. A closer examination found that the stronger front-to-rear outflow usually occurred over the top of the convective cores while the weaker rear-to-front outflow dominated over the rest of the areas including the stratiform region (not shown). The net effect of the high-frequency weak front-to-rear outflows and the low-frequency strong rear-to-front outflows was to offset the magnitude of the mean profile.

Because of the uncertainty of vertical velocity at higher elevations, only CFAD and mean profiles of the horizontal divergence field will be discussed. Comparing the divergence CFADs, we found the modes of the distributions were identical for the convection in the pre- and postfrontal region (Figs. 10g and 10h). When the low-level convergence is very important to the development of convection, it was noticed that the low-level divergence field had a wider distribution at 0930 UTC. This indicated a higher relative frequency of occurrence of intense convergence at low levels at that time. The mean divergence profiles showed that the layer of average convergence was shallower ($\sim$4.5 km MSL) at 0620 UTC and deeper ($\sim$9 km MSL) at 0930 UTC (Figs. 10i and 10j). The deeper layer of average convergence in the postfrontal region attributed to the strong interaction between the northerly frontal airflow from the midlatitude and the southerly monsoon flow from the Tropics. The deeper and stronger low-level average convergence may also contribute to a much taller convection in the postfrontal region.

6. Summary

In this study, the evolution and structure of mesoscale convection in the SCS region are documented for the first time. In particular, this paper focuses on the convection associated with the frontal passage at the early stage of the summer SEAM onset. From the case of 15 May 1998, it was found that the interaction between the tropical monsoon flow and the frontal circulation played an important role in the evolution and structure of the mesoscale convection. In the prefrontal region, the maintenance and intensification of the convection relied

on the low-level convergence of the different component of the southwesterly winds including the southwesterly monsoon flow and the prefrontal southwesterly flow. The north-to-south-oriented primary convective line was perpendicular to the low-level wind shear, and the east–west-oriented secondary convective lines were parallel to the low-level shear. This was in agreement with the conclusion made by LeMone et al. (1998) from their studies of western Pacific convection when the low-level wind shear is over 4 m s^{-1}. In the postfrontal region, strong convection formed in an east-to-west zone where the southwesterly monsoon flow converged with the northerly postfrontal flow. The strong low-level convergence generated by the two branches of airflow at the opposite direction may help the postfrontal convection to be more intense and taller than the prefrontal convection.

The structure of the mesoscale convection observed on 15 May shared some similarities with archetypal tropical oceanic convection documented in other geographical regions: 1) the low-level inflow from the warm and moist air ahead of the leading edge, 2) the maximum radar reflectivity at the lowest levels, 3) the strong reflectivity gradient above the 0°C isotherm implying a relative weak updraft, 4) generally an elevated (over 7.5 km MSL) vertical velocity maximum. However, significant departures were also evident: 1) a more vertical radar echo and updraft pattern with little tilt in the prefrontal region with a moderate vertical wind shear, 2) very limited stratiform rain in an intense convection due to a very dry mid to upper layer resulting in a quick evaporation and sublimation, 3) a leading stratiform mode instead of the more frequent trailing stratiform mode (Houze 1977; Protat and Lemaitre 2001), and 4) a maximum low-level convergence and updraft in the rear portion of the prefrontal convection related to the more vertical convection. It is interesting to note that the kinematic structures resulting in the leading stratiform rain were different from prefrontal to postfrontal convection. In the prefrontal region, the leading stratiform rain was caused by a rear-to-front midlevel outflow blowing hydrometers forward, and the dry environmental air in upper levels also prevented the formation of stratiform rain there. In the postfrontal region, in contrast to most tropical convection (Lewis et al. 1998), the low-level inflow did not go to the upper-rear part of convection but turned forward at the layer above 7.5 km. Thus, the leading stratiform rain formed as a result of forward advection of the hydrometers.

From a statistical viewpoint, similarities and differences also existed between the pre- and postfrontal convection as well as compared to other tropical oceanic convection. The distribution and mean profile of the radar reflectivity for these convective systems were very similar at the lowest levels with the maximum reflectivity recorded. However, in the prefrontal region, the mean radar reflectivity had a higher decrease rate with height in the layers below the freezing level. Above the freezing level, a rapid decrease in reflectivity was found, as in other tropical monsoon convections (Williams et al. 1992; Zipser and Lutz 1994), suggesting a mild updraft in the convection. The postfrontal convection had a significantly higher frequency of occurrence of intense echoes at the upper level, implying that the postfrontal convection would likely produce a higher rain rate. Compared to the results from GATE and TAMEX, the mean radar reflectivity profile of the postfrontal convection was very similar to that documented in earlier studies. Obvious differences in system-relative winds existed at the upper levels for the pre- and postfrontal convection. For the prefrontal convection, the convective-driven outflows at the upper level were very strong. For the postfrontal convection, the system-relative flows at the upper level consisted of relatively weak front-to-rear winds over the large stratiform region and relatively strong rear-to-front winds over the small convective region. Strong low-level convergence had a higher probability of occurrence for the postfrontal convection. The postfrontal convection also had a deep 9-km convergence layer, compared to only a 4-km convergence layer for the prefrontal convection. Apparently, the low-level convergence generated by the northerly frontal flows and southerly monsoon flows in the postfrontal regime is more pronounced than the convergence produced by two branches of southwesterly flows in the prefrontal regime.

REFERENCES

Akiyama, T., 1979: Thermal stratification in baiu frontal medium-scale disturbances with heavy rainfalls. *J. Meteor. Soc. Japan,* **57,** 267–283.

——, 1984: A medium-scale cloud cluster in a baiu front. Part I: Evolution process and fine structure. *J. Meteor. Soc. Japan,* **62,** 485–504.

Anagnostou, E. N., C. A. Morales, and T. Dinku, 2001: The use of TRMM Precipitation Radar observations in determining ground radar calibration biases. *J. Atmos. Oceanic Technol.,* **18,** 616–628.

Barnes, G. M., and K. Sieckman, 1984: The environment of fast- and slow-moving tropical mesoscale convective cloud lines. *Mon. Wea. Rev.,* **112,** 1782–1794.

Biggerstaff, M. I., and R. A. Houze Jr., 1991: Kinematic and precipitation structure of the 10–11 June 1985 squall line. *Mon. Wea. Rev.,* **119,** 3035–3065.

Carey, L. D., S. A. Rutledge, D. A. Ahijevych, and T. D. Keenan, 2000: Correcting propagation effects in C-band polarimetric radar observation of tropical convection using differential propagation phase. *J. Appl. Meteor.,* **39,** 1405–1433.

Chang, C.-P., and T. N. Krishnamurti, 1987: *Monsoon Meteorology,* Oxford University Press, 353 pp.

Chen, Y.-L., and N. B.-F. Hui, 1992: Analysis of a relatively dry front during the Taiwan Area Mesoscale Experiment. *Mon. Wea. Rev.,* **120,** 2442–2468.

Cho, H.-R., and G. T. J. Chen, 1995: Mei-yu frontogenesis. *J. Atmos. Sci.,* **52,** 2109–2120.

Davies-Jones, R. P., 1979: Dual-Doppler radar coverage area as a function of measurement accuracy and spatial resolution. *J. Appl. Meteor.,* **18,** 1229–1233.

DeMott, C. A., and S. A. Rutledge, 1998: The vertical structure of TOGA COARE convection. Part I: Radar echo distributions. *J. Atmos. Sci.,* **55,** 2730–2747.

Ding, Y., 1994: *Monsoons over China.* Kluwer Academic, 419 pp.

——, and Y. Liu, 2001: Onset and the evolution of the summer monsoon over the South China Sea during SCSMEX field experiment in 1998. *J. Meteor. Soc. Japan,* **79,** 255–276.

Drosdowsky, W., G. J. Holland, and R. K. Smith, 1989: Structure and evolution of north Australian cloud lines observed during AMEX phase I. *Mon. Wea. Rev.,* **117,** 1181–1192.

Fein, J. S., and J. P. Kuettner, 1980: Report on the summer MONEX field phase. *Bull. Amer. Meteor. Soc.,* **61,** 461–474.

Fu, C.-B., J. Fletcher, and R. Slutz, 1983: The structure of the Asian monsoon surface wind field over the ocean. *J. Climate Appl. Meteor.,* **22,** 1242–1252.

Fukao, S., M. D. Yamanaka, T. Sato, T. Tsuda, and S. Kato, 1988: Three-dimensional air motions over the baiu front observed by a VHF-band Doppler radar: A case study. *Mon. Wea. Rev.,* **116,** 281–292.

Grossman, R. L., and D. R. Durran, 1984: Interaction of low-level flow with the western Ghat Mountains and offshore convection in the summer monsoon. *Mon. Wea. Rev.,* **112,** 652–672.

He, H., J. W. McGinnis, Z. S. Song, and M. Yanai, 1987: Onset of the Asian summer monsoon in 1979 and the effect of the Tibetan Plateau. *Mon. Wea. Rev.,* **115,** 1966–1995.

Holland, G. J., J. L. McBride, R. K. Smith, D. Jasper, and T. D. Keenan, 1986: The BMRC Australian Monsoon Experiment: AMEX. *Bull. Amer. Meteor. Soc.,* **67,** 1466–1472.

Houze, R. A., Jr., 1977: Structure and dynamics of a tropical squall-line system. *Mon. Wea. Rev.,* **105,** 1540–1567.

——, and C.-P. Cheng, 1977: Radar characteristics of tropical convection observed during GATE: Mean properties and trends over the summer monsoon. *Mon. Wea. Rev.,* **105,** 964–980.

Johnson, R. H., and P. E. Ciesielski, 2002: Characteristics of the 1998 summer monsoon onset over the northern South China Sea. *J. Meteor. Soc. Japan,* **80,** 561–578.

——, and T. Keenan, 2001: Organization of oceanic convection during the onset of the 1998 east Asia summer monsoon. Preprints,

30th Int. Conf. on Radar Meteorology, Munich, Germany, Amer. Meteor. Soc., 679–681.

Jorgensen, D. P., and M. A. LeMone, 1989: Vertical velocity characteristics of oceanic convection. *J. Atmos. Sci.,* **46,** 621–640.

——, ——, and S. B. Trier, 1997: Structure and evolution of the 22 February 1993 TOGA COARE squall line: Aircraft observations of precipitation, circulation, and surface energy fluxes. *J. Atmos. Sci.,* **54,** 1961–1985.

Kawatani, Y., and M. Takahashi, 2003: Simulation of the baiu front in a high resolution AGCM. *J. Meteor. Soc. Japan,* **81,** 113–126.

Krishnamurti, T. N., 1985: Summer monsoon experiment—A review. *Mon. Wea. Rev.,* **113,** 1590–1626.

Kummerow, C., and Coauthors, 2000: The status of the Tropical Rainfall Measuring Mission (TRMM) after two years in orbit. *J. Appl. Meteor.,* **39,** 1965–1982.

Lau, K.-M., G. J. Yang, and S. H. Shen, 1988: Seasonal and intraseasonal climatology of summer monsoon rainfall over east Asia. *Mon. Wea. Rev.,* **116,** 18–37.

——, and Coauthors, 2000: Report of the field operations and early results of the South China Sea Monsoon Experiment (SCSMEX). *Bull. Amer. Meteor. Soc.,* **81,** 1261–1270.

——, X. Li, and H.-T. Wu, 2002: Evolution of the large scale circulation, cloud structure and regional water cycle associated with the South China Sea monsoon during May–June, 1998. *J. Meteor. Soc. Japan,* **80,** 1129–1147.

Leise, J. A., 1981: A multidimensional scale-telescoped filter and data extension package. NOAA Tech. Memo. ERL WPL-82, 18 pp.

LeMone, M. A., and E. J. Zipser, 1980: Cumulonimbus vertical velocity events in GATE. Part I: Diameter, intensity and mass flux. *Mon. Wea. Rev.,* **108,** 2444–2457.

——, G. M. Barnes, E. J. Szoke, and E. J. Zipser, 1984: The tilt of the leading edge of mesoscale tropical convective lines. *Mon. Wea. Rev.,* **112,** 510–519.

——, E. J. Zipser, and S. B. Trier, 1998: The role of environmental shear and thermodynamic conditions in determining the structure and evolution of mesoscale convective systems during TOGA COARE. *J. Atmos. Sci.,* **55,** 3493–3518.

Lewis, S. A., M. A. LeMone, and D. P. Jorgensen, 1998: Evolution and dynamics of a late-stage squall line that occurred on 20 February 1993 during TOGA COARE. *Mon. Wea. Rev.,* **126,** 3189–3212.

Li, J., Y.-L. Chen, and W.-C. Lee, 1997: Analysis of a heavy rainfall event during TAMEX. *Mon. Wea. Rev.,* **125,** 1060–1082.

Mohr, C. G., L. J. Miller, R. L. Vaughan, and H. W. Frank, 1986: The merger of mesoscale datasets into a common Cartesian format for efficient and systematic analyses. *J. Atmos. Oceanic Technol.,* **3,** 143–161.

Moncrieff, M. W., 1992: Organized convective systems: Archetypal dynamical models, mass and momentum flux theory, and parameterization. *Quart. J. Roy. Meteor. Soc.,* **118,** 819–850.

Murakami, T., and Y. H. Ding, 1982: Wind and temperature changes over Eurasia during the early summer of 1979. *J. Meteor. Soc. Japan,* **60,** 183–196.

Nagata, M., and Y. Ogura, 1991: A modeling case study of interaction between heavy precipitation and a low-level jet over Japan in the baiu season. *Mon. Wea. Rev.,* **119,** 1309–1336.

Ninomiya, N., 1984: Characteristics of baiu front as a predominant subtropical front in the summer Northern Hemisphere. *J. Meteor. Soc. Japan,* **62,** 880–894.

——, and T. Akiyama, 1971: The development of the medium-scale disturbance in the baiu front. *J. Meteor. Soc. Japan,* **49,** 663–677.

——, and T. Murakami, 1987: The early summer rainy season (baiu) over Japan. *Monsoon Meteorology,* C.-P. Chang, and T. N. Krishnamurti, Eds., Oxford University Press, 93–121.

Oye, R., and R. E. Carbone, 1981: Interactive Doppler editing software. Preprints, *20th Conf. on Radar Meteorology,* Boston, MA, Amer. Meteor. Soc., 683–689.

Parker, M. D., 2002: Dynamics of convective lines with leading precipitation. Preprints, *21st Conf. on Severe Local Storms,* San Antonio, TX, Amer. Meteor. Soc., 5–8.

——, and R. H. Johnson, 2000: Organizational modes of midlatitude mesoscale convective systems. *Mon. Wea. Rev.,* **128,** 3413–3436.

——, and ——, 2001: Simple numerical simulation of convective lines with leading stratiform precipitation. Preprints, *Ninth Conf. on Mesoscale Processes,* Fort Lauderdale, FL, Amer. Meteor. Soc., 283–287.

Protat, A., and Y. Lemaitre, 2001: Scale interaction involved in the initiation, structure, and evolution of the 15 December 1992 MCS observed during TOGA COARE. Part II: Mesoscale and convective-scale processes. *Mon. Wea. Rev.,* **129,** 1779–1808.

Rickenbach, T. M., and S. A. Rutledge, 1998: Convection in TOGA COARE: Horizontal scale, morphology, and rainfall production. *J. Atmos. Sci.,* **55,** 2715–2729.

Rotunno, R., and J. B. Klemp, 1982: The influence of the shear induced pressure gradient on thunderstorm motion. *Mon. Wea. Rev.,* **110,** 136–151.

——, ——, and M. L. Weisman, 1988: A theory for strong, long-lived squall lines. *J. Atmos. Sci.,* **45,** 463–485.

Rutledge, S. A., E. R. Williams, and T. D. Keenan, 1992: The Down Under Doppler and Electricity Experiment (DUNDEE): Overview and preliminary results. *Bull. Amer. Meteor. Soc.,* **73,** 3–16.

Ryzhkov, A. V., and D. S. Zrnic, 1998: Polarimetric rainfall estimation in the presence of anomalous propagation. *J. Atmos. Oceanic Technol.,* **15,** 1320–1330.

Smith, R. B., and Y. Lin, 1984: Orographic rain on the western Ghats. *Proceedings of the First Sino-American Workshop on Mountain Meteorology,* E. R. Reiter, B. Zhu, and Y. Qian, Eds., Science Press and Amer. Meteor. Soc., 71–94.

Tao, S., and L. Chen, 1987: A review of recent research on the east Asian summer monsoon in China. *Monsoon Meteorology,* C.-P. Chang, and T. N. Krishnamurti, Eds., Oxford University Press, 60–92.

Trier, S. B., W. C. Skamarock, M. A. LeMone, D. B. Parsons, and D. P. Jorgensen, 1996: Structure and evolution of the 22 February 1993 TOGA COARE squall line: Numerical simulations. *J. Atmos. Sci.,* **53,** 2861–2886.

Tu, Z.-W., and S.-S. Huang, 1944: The advance and retreat of the summer monsoon. *Meteor. Mag.,* **18,** 1–20.

Wakimoto, R. M., 1982: The life cycle of thunderstorm gust fronts as viewed with Doppler radar and rawinsonde data. *Mon. Wea. Rev.,* **110,** 1060–1082.

——, C. Liu, and H. Cai, 1998: The Garden City, Kansas, storm during VORTEX 95. Part I: Overview of the storm's life cycle and mesocyclogenesis. *Mon. Wea. Rev.,* **126,** 372–392.

Wang, J.-J., 2001: The development and structure of an oceanic squall line systems during the South China Sea Summer Monsoon Experiment. Preprints, *30th Int. Conf. on Radar Meteorology,* Munich, Germany, Amer. Meteor. Soc., 400–402.

Weisman, M. L., 1992: The role of convectively generated rear-inflow jets in the evolution of long-lived mesoconvective systems. *J. Atmos. Sci.,* **49,** 1826–1847.

Williams, E. R., S. A. Rutledge, S. G. Geotis, N. Renno, E. Rasmussen, and T. Rickenbach, 1992: A radar and electrical study of tropical "hot towers." *J. Atmos. Sci.,* **49,** 1386–1395.

Yuter, S. E., and R. A. Houze, Jr., 1995: Three-dimensional kinematic and microphysical evolution of Florida cumulonimbus. Part II: Frequency distributions of vertical velocity, reflectivity, and differential reflectivity. *Mon. Wea. Rev.,* **123,** 1941–1963.

Zhu, K., 1934: Monsoon in southeast Asia and rainfall amount in China. *Acta Geogr. Sin.,* **1,** 1–27.

Zipser, E. J., 1977: Mesoscale and convective-scale downdrafts as distinct components of squall-line structure. *Mon. Wea. Rev.,* **105,** 1568–1589.

——, and M. A. LeMone, 1980: Cumulonimbus vertical velocity events in GATE. Part II: Synthesis and model core structure. *J. Atmos. Sci.,* **37,** 2458–2469.

——, and K. Lutz, 1994: The vertical profile of radar reflectivity of convective cells: A strong indicator of storm intensity and lightning probability? *Mon. Wea. Rev.,* **122,** 1751–1759.